Solid Deep Ultraviolet Diffracting Inverse Opal Photonic Crystals
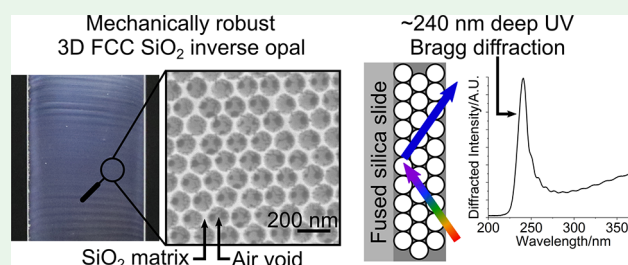
Kyle T. Hufziger,[ID] Alyssa B. Zrimsek,[ID] and Sanford A. Asher*[ID]

Department of Chemistry, University of Pittsburgh, Pittsburgh, Pennsylvania 15260, United States

Ⓢ Supporting Information

ABSTRACT: We fabricated the first solid, mechanically robust inverse opal photonic crystals that diffract in the deep ultraviolet (UV) spectral region. These photonic crystals are fabricated by self-assembling <140 nm diameter monodisperse polystyrene nanoparticles into face centered cubic 3D close-packed structures on fused silica microscope slides in the presence of tetraethyl orthosilicate via a vertical deposition method. Tetraethyl orthosilicate condenses in the nanoparticle interstices during self-assembly, immobilizing the polystyrene nanoparticles in an SiO_2 matrix. Removal of the polystyrene nanoparticles using piranha solution yields a stable SiO_2 inverse opal structure that Bragg diffracts in the deep UV at <245 nm. We measured the UV−vis transmission, diffraction of a collimated deep UV white light source, and diffraction of 229 nm laser light in order to characterize the deep UV optical performance of these photonic crystals. We measured a maximum light attenuation of ∼98% at the Bragg condition, calculated a photonic crystal thickness of ∼33 layers, and calculated a diffraction spectral bandwidth of 16.8 nm full-width at half-maximum. The mechanical robustness, photochemical durability, and shelf life of the deep UV diffracting photonic crystals demonstrated in this work enable their development for use as deep UV optical devices. We conclude that additional optimization of the self-assembly and vertical deposition conditions is required to improve the thickness uniformity and ordering of these photonic crystals to increase their diffraction efficiency and to decrease their diffraction bandwidth.

KEYWORDS: ultraviolet diffraction, photonic crystal, inverse opal, vertical deposition, convective self-assembly, nanoparticles

Mechanically robust 3D FCC SiO_2 inverse opal

~240 nm deep UV Bragg diffraction

SiO_2 matrix — Air void

Fused silica slide

Diffracted Intensity/A.U.

200 250 300 350 Wavelength/nm

INTRODUCTION

The development of spectroscopic techniques utilizing deep ultraviolet (UV) (<300 nm) light is significantly impeded by the scarcity of optics that operate in this spectral region. High performance optics, such as narrow and broadband dielectric mirrors, as well as Rayleigh rejection filters for Raman spectroscopy, are commercially available throughout the near-UV, visible, and near-IR spectral regions. However, the availability of such optics in the deep UV is extremely limited, especially for Rayleigh rejection optical devices at wavelengths of <250 nm. In addition, the performance of deep UV optics is generally challenged by the absorption of many materials in the deep UV.[1]

Limited deep UV optic availability greatly complicates construction of deep UV Raman instruments. The lack of Rayleigh rejection optics impedes development of deep UV Raman spectroscopy by necessitating the use of multiple monochromator stages to remove the intense Rayleigh scattered light. This drastically decreases light throughput and requires long accumulation times during spectral collection.[2−4] In addition to the lack of deep UV rejection filters for Raman spectroscopy, the lack of optics that are capable of transmitting or diffracting narrow bandwidth spectral regions in the deep UV, such as liquid crystal tunable filters (LCTFs), acousto-optic tunable filters (AOTFs), and dielectric notch filters, strongly hinders the development of deep UV wide-field imaging spectroscopies that require these

devices.[5] These devices are frequently utilized in the visible and near-IR spectral regions to select a narrow bandwidth spectral region to focus onto a detector and form a wide-field image. Unfortunately, to our knowledge these wavelength selecting devices have not previously been manufactured in the deep UV spectral region.

Our group recently developed the first deep UV diffracting photonic crystals (PCs) that function as Rayleigh rejection filters for 229 nm excited Raman measurements and as the wavelength selection device in the first 229 nm wide-field Raman imaging spectrometer for standoff trace explosive detection.[1,6] In our previous work, we synthesized highly charged, monodisperse silica nanoparticles via modified Stöber methods. After removal of electrolytes and other impurities that screen electrostatic interactions, these highly charged nanoparticles self-assemble via electrostatic repulsion to form aqueous non-close-packed face centered cubic (FCC) colloidal crystals that diffract narrow bandwidth spectral regions in the deep UV. Further development of deep UV diffracting PCs would enable their commercialization as Rayleigh rejection optics, optical filters, wide-field imaging optics, and dielectric-style or dichroic-style mirrors that reflect particular wavelengths only at certain angles.

The current challenge for the development of PCs for use in deep UV spectroscopic instrumentation is that the electrostatically stabilized colloidal crystals composed of silica nanoparticles in water are relatively fragile. Aqueous PCs can be transiently disordered by deep UV laser-induced photochemistry that produces ions that screen interparticle repulsions. In addition, PC ordering can be disrupted by mechanical vibrations, temperature variations, and solvent evaporation.

Several strategies can be employed to improve PC stability and shelf life. For example, PC durability can be improved by polymerizing a matrix around the FCC nanoparticle array, embedding the nanoparticles in a polymer film that resists disorder.[7−9] Utilizing this approach to fabricate deep UV diffracting PCs is challenging since the nanoparticles and polymer matrix must be transparent in the deep UV.[10] Nanoparticles can also be self-assembled into 2D or 3D close-packed structures by using various evaporative techniques, producing solventless PCs on solid substrates.[11−15]

Here, we explore the fabrication of inverse opals (IOs) that form solventless, indefinitely shelf stable deep UV diffracting PCs. IO PCs are typically fabricated by filling the interstices of a 3D nanoparticle PC with a liquid monomer, sol−gel precursor, or mineral precursor solution, which is then polymerized or crystallized, embedding the nanoparticles in a solid matrix.[16−21] Removal of the nanoparticles by either dissolution or calcination while preserving the interstitial matrix yields the final IO PC. This IO PC structure consists of an ordered array of voids left after nanoparticle removal.

Recently, Hatton et al. developed a coassembly vertical deposition method wherein self-assembly of a 3D close-packed FCC array of polymer nanoparticles occurs on a vertical substrate in the presence of tetraethyl orthosilicate (TEOS), a sol−gel precursor that condenses during self-assembly to form an SiO_2 matrix within the nanoparticle interstices.[18] Calcination of the PCs in an oven at 500 °C removed the polymer nanoparticles while leaving the SiO_2 matrix mostly intact, yielding an IO PC structure.

In this work, we utilized the deep UV transparency and mechanical strength of SiO_2 to fabricate the first mechanically robust, solventless deep UV diffracting IO PCs by using a modified coassembly vertical deposition method. To create these IO PCs, we first vertically deposit 138.3 ± 3.1 nm diameter polystyrene nanoparticles (PSNPs) into a 3D close-packed FCC structure on a fused silica microscope slide in the presence of TEOS. This results in a PSNP FCC structure embedded in an SiO_2 matrix. We then react these PSNP/SiO_2 PCs with piranha solution to dissolve the PSNPs, forming IO PCs that Bragg diffract light in the deep UV. Importantly, these IO PCs are stable and show no diffraction degradation during handling or UV laser irradiation. We investigate the diffraction and morphology of these PCs to determine their ordering and utility as deep UV PC diffraction devices.

■ EXPERIMENTAL SECTION

3D Close-Packed PSNP/SiO₂ PC Self-Assembly and IO PC Formation. For terminology, "PSNP/SiO_2 PCs" shall be used when referring specifically to solid 3D close-packed FCC PCs containing PSNPs surrounded by an SiO_2 matrix formed by vertical deposition. "IO PCs" shall be used when referring specifically to PSNP/SiO_2 PCs after treatment with piranha to remove the PSNPs, yielding an FCC array of voids surrounded by an SiO_2 matrix.

We synthesized 138.3 ± 3.1 nm diameter monodisperse, highly charged PSNPs (Figure S1) via a modified[22] emulsion polymerization

procedure[23] (see Supporting Information for synthesis details). We measured a ζ-potential of −49.5 mV at pH 5.0. These nanoparticles were self-assembled to form 3D close-packed PCs on fused silica substrates utilizing a modified vertical deposition procedure based on the method of Hatton et al.[18]

3 in. × 1 in. fused silica microscope slides (Technical Glass Products 80/50 scratch dig, 1 mm thick) were cut into ∼50 mm × 12 mm pieces using a glass saw. Directly before use the 50 mm × 12 mm substrate was immersed in freshly prepared 3:1 v/v H_2SO_4/H_2O_2 (Fisher Scientific A300 96% w/w and Fisher Scientific H323 30%) piranha solution to remove surface contaminants and increase substrate hydrophilicity. *Safety warning: Piranha solution becomes extremely hot upon mixing, is a powerful oxidizer, reacts rapidly with organics, and produces gases. Make only in small quantities as needed and use appropriate protective equipment.* After several hours of soaking, the substrate was removed from piranha, immediately rinsed with nanopure H_2O (Thermo Scientific Barnstead), and stored in nanopure H_2O until use.

A dilute PSNP solution was prepared by first centrifuging an aliquot of stock colloid solution at 1000 relative centrifugal force (RCF) for 1 min to spin-down ion-exchange resin beads. Following centrifugation, an aliquot of stock colloid solution was diluted with nanopure H_2O to produce a 21.00 mL solution, typically containing 0.18% v/v PSNPs, in a 20 mL (nominal volume) scintillation vial (Fisher Scientific 03-337-14 borosilicate, 61 mm × 28 mm height × outer diameter). Fresh 0.1 M HCl (Fisher Scientific A144S, 37% w/w) was prepared in nanopure H_2O. A TEOS solution was freshly prepared by mixing 800 μL of 0.1 M HCl solution, 1520 μL of ethanol (Decon Labs 200 proof), and 812 μL of tetraethyl orthosilicate (TEOS, Sigma-Aldrich 86578, >99%). The TEOS solution was sealed and mixed for ∼1 h until use to allow time for HCl catalyzed hydrolysis of TEOS.[24]

The vertical deposition setup was prepared as follows. An oven (Thermo Scientific Heratherm IMH-60) situated on a floated optical table (Kinetic Systems Vibraplane) was heated to ∼48.3 °C. The temperature and humidity in the oven were recorded by using a hygrometer probe (Traceable Hygrometer 11-661-7B) situated next to the deposition vials on the top shelf of the oven. The oven fan was set at the lowest speed (20% setting) to gently circulate oven air. Oven air was slowly and continually refreshed during the experiment by purging the oven with 2.6 standard liters per minute (SLPM) dry N_2 gas. The N_2 line was run through the open oven accessory port on the top/back of the oven, with the line outlet situated on the bottom shelf of the oven.

A 225 μL aliquot of TEOS solution was added to the 21.00 mL of dilute PSNP solution and mixed. A piranha cleaned fused silica substrate stored in nanopure H_2O was rinsed with fresh nanopure H_2O and placed in the scintillation vial containing the PSNP solution and TEOS solution. The vial containing the fused silica substrate was then placed into the preheated oven. The oven was then closed, and self-assembly of the 3D close-packed FCC array was allowed to proceed undisturbed for 4 days. Typical oven humidity values ranged from ∼11% relative humidity at the beginning of self-assembly to ∼2% when the solution was nearly evaporated. The oven temperature was maintained within ±0.2 °C of its median value during self-assembly. After evaporation of most of the PSNP/TEOS solution, the fused silica substrates with attached close-packed PSNP/SiO_2 PCs were removed from the oven and placed into clean vials for storage.

To remove the PSNPs from the PSNP/SiO_2 PCs while leaving the surrounding SiO_2 matrix intact, we completely immersed the PSNP/SiO_2 PCs in freshly prepared 3:1 v/v piranha solution overnight. After soaking, the PCs were removed from piranha and immersed in a vial of nanopure H_2O. The H_2O was changed once to wash away remaining acid, and the PCs were then allowed to air-dry before use, yielding the final IO PCs. A schematic of the fabrication method is depicted in Figure 1.

Nanoparticle and PC Characterization. PSNP diameters (Figure S1) were measured by evaporating a small aliquot of dilute colloidal dispersion onto a Formvar coated Cu grid (Ted Pella 01814-F) before imaging with a transmission electron microscope (FEI
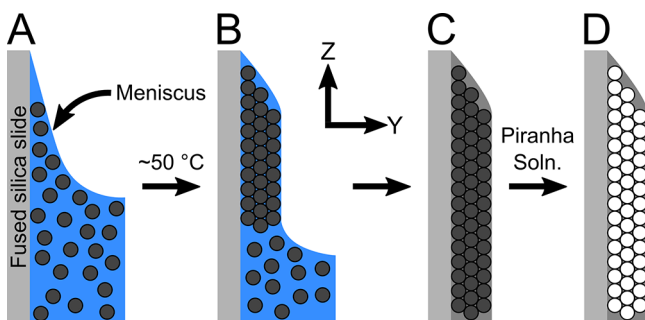
Figure 1. Schematic of the deep UV diffracting IO PC fabrication method. (A) A clean, hydrophilic fused silica substrate is dipped into a solution, depicted in blue, containing PSNPs, TEOS, ethanol, HCl, and water in a 20 mL vial. The vial is then placed in a hot oven. (B) Self-assembly of the 3D close-packed FCC PSNP structure onto the fused silica substrate proceeds via evaporation driven vertical deposition over several days while TEOS condenses in the PSNP interstices to form an SiO$_2$ matrix. (C) After drying, the PSNPs are embedded in an SiO$_2$ matrix that is attached to the fused silica substrate. (D) Piranha solution is used to remove the PSNPs while leaving the SiO$_2$ intact, yielding an FCC array of voids in the SiO$_2$ matrix.

Morgagni 268). >100 nanoparticle diameters were measured via ImageJ (NIH) software to determine the size distribution of the particles. The ζ-potential of the PSNPs was measuring using a Malvern ZS-90 Zetasizer (Smoluchowski approximation).

IO PC ordering (Figure 2) was monitored using a scanning electron microscope (SEM) (Ziess Sigma 500 VP FE-SEM) in SEI mode at 3 kV accelerating voltage after sputter coating the PCs with Au (Pelco SC-7). The average IO PC void diameter was determined by measuring the distance between the centers of neighboring SiO$_2$ void walls in scanning electron micrographs (>100 voids measured).

Optical transmission in the near and deep UV (Figure 3) was measured using a Varian Cary 5000 UV−vis−NIR absorption spectrometer. The PCs were mounted on a rotational stage (Newport 481-A) placed within the spectrometer. The rotational stage was utilized to vary the incident angle of light on the PCs to monitor the Bragg diffraction wavelength as a function of angle. All spectra were baseline corrected where the blank was a clean fused silica microscope slide at normal incidence.

To measure Fabry−Perot interference fringes and determine IO PC thickness (Figure 4), 170−2100 nm white light from a laser driven light source (LDLS, Energetiq EQ-99X) was collimated by an off-axis parabolic mirror (Thor Labs MPD249-F01) and directed through an aperture that reduced the beam diameter to 6 mm before illuminating the IO PC. The IO PC was mounted to a microscope slide holder attached to a rotational stage (Newport 481-A) to control the beam incident angle onto the IO PC. Light diffracted by the IO PC was collected by a reflective collimator (Thor Labs RC12SMA-F01), which is a 90° off-axis parabolic mirror. The reflective collimator was utilized to collect and focus the diffracted light into an optical fiber (Thor Labs M22L02). The optical fiber then directed the diffracted light into the slit of a deep UV optimized Ocean Optics QE Pro spectrometer. The IO PC diffraction spectrum shown in Figure 4 was produced by dividing the raw diffraction spectrum by the spectrum of the LDLS lamp light reflected from a clean fused silica slide to correct for the instrument throughput and the source spectral shape.

To directly measure the Bragg diffraction bandwidth of the IO PCs, we measured the angular dependence of 229 nm light diffraction (Figure 5). Collimated 229 nm light was generated by a continuous wave frequency doubled Ar ion laser (Coherent Innova 300c FreD). A fused silica slide was placed in the incident beam path at an oblique angle to pick off a small portion of the beam, which was measured by a photodiode power sensor (Thor Labs S120VC head attached to a PM200 meter) that continuously monitored the incident power. The beam was then directed through an aperture to produce a 3 mm

diameter circular beam at the IO PC. The IO PC was mounted to a motorized rotational stage (Zaber X-RSW60A) to allow precise, reproducible rotation about the z-axis (Figure 2A) of the IO PC. The IO PC was rotated in 0.50° increments, and light diffracted at each incident angle was measured by a second photodiode power sensor (Thor Labs S120VC), positioned at each measurement angle to center the diffracted beam on the sensor head. At each IO PC angle the diffracted power and pick-off power were measured simultaneously for several seconds (∼50 data points per meter per angle, Thor Labs Multi Power Meter Utility) to average out any laser power variations. The measured pick-off power was utilized to calculate the incident power on the sample. The diffracted power was divided by the calculated incident power to determine the fraction of power diffracted by the IO PC at each incident angle.

IO PC surface roughness (Figure 6B) was quantified using an optical profilometer (Bruker Contour GT-I). Height maps collected using the profilometer were tilt corrected using the instrument software (Bruker Vision64).

■ RESULTS AND DISCUSSION

Fabrication Parameters and SEM Analysis. We fabricated the first solid deep UV diffracting IO PCs. To accomplish this, we modified previous vertical deposition methods to optimize the self-assembly of small diameter 138.3 ± 3.1 nm diameter PSNPs (Figure S1) into close-packed FCC PCs.[18] To improve the self-assembly of these close-packed PSNP/SiO$_2$ PCs and to improve the deep UV diffraction, we optimized the oven humidity and temperature, PSNP concentration, volume of TEOS solution, and vial/substrate size used during the vertical deposition.

We found that the vial size is crucially important to produce IO PCs that efficiently diffract in the deep UV. We could reproducibly and easily fabricate IO PCs with strong deep UV diffraction by using 20 mL scintillation vials or smaller, 3-dram vials (using smaller substrates) under similar solution and oven conditions. However, it was difficult to obtain good deep UV diffraction for PCs fabricated using 3 in. × 1 in. fused silica substrates placed in larger 50 mL vials. A deep UV diffracting IO PC was fabricated on a 3 in. × 1 in. substrate at a lower ∼31 °C oven temperature; however the IO PC visually appeared very heterogeneous and showed broad diffraction peaks when measured using the absorption spectrometer, indicating that the nanoparticle ordering was generally poor.

The self-assembly mechanism of 3D close-packed structures on solid substrates via vertical deposition is still somewhat poorly understood.[25−28] It is hypothesized that vertical deposition of 3D arrays occurs because the relative evaporation rate from the thin, top part of the solution meniscus near the substrate−air−solution contact line is faster than from the bulk solution (Figure 1).[26] Relatively rapid evaporation from the solution meniscus results in a convective solvent flow that continuously draws nanoparticles into the meniscus toward the contact line. It is hypothesized that interparticle capillary forces or convective steering due to solvent flow through nanoparticle interstices draws particles together into a close-packed array that grows as the contact line moves along the substrate z-axis due to continuous solvent evaporation.[28−30]

The rate of evaporation of the solution relative to the rate of particle influx into the meniscus must be carefully balanced to produce highly ordered 3D close-packed structures. For example, Kaplan et al. previously found that continuous, well-ordered vertically deposited arrays only formed when above a certain critical nanoparticle concentration.[26] We hypothesize that the relatively rapid solution evaporation
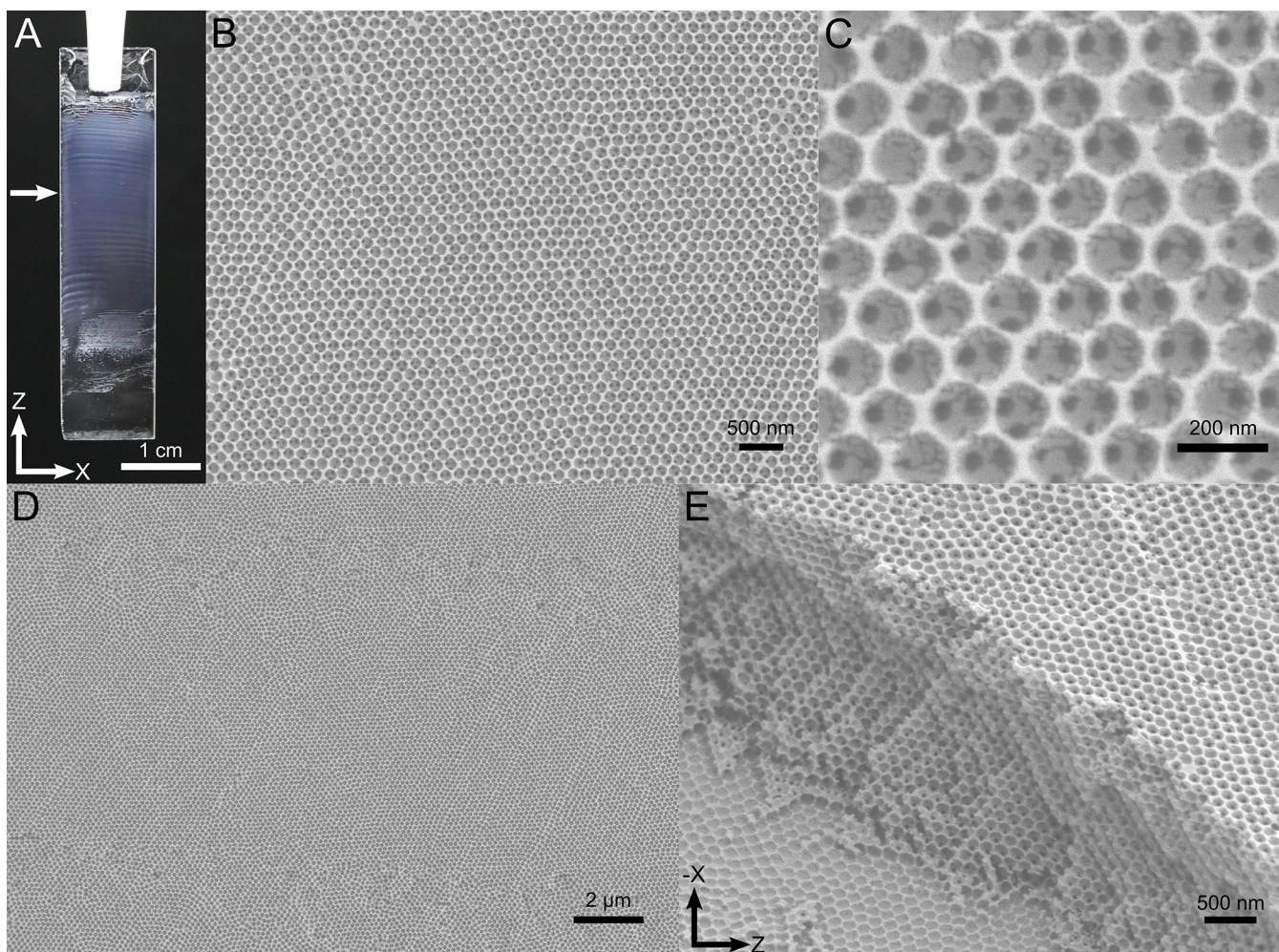
Figure 2. Photograph and SEM micrographs all originating from the same IO PC. (A) Photograph of an IO PC after piranha solution treatment to remove PSNPs. Arrow indicates strongly diffracting region. (B−D) SEM micrographs of the strongly diffracting region of the IO PC shown in panel A. Each micrograph axis orientation is the same as shown in panel A. (E) SEM micrograph of the same IO PC sample tilted 45°, showing the inner structure of a delaminated region at the edge of the fused silica substrate. SEM micrographs of a similar PSNP/SiO$_2$ PC sample prior to sphere removal are shown in Figure S2.

caused by the wide aperture of the 50 mL vial confounds selection of appropriate deposition conditions to produce highly ordered IO PCs.

We utilized piranha solution to remove the PSNPs instead of tetrahydrofuran (THF) or toluene, which is generally used to dissolve PSNPs, because we found that the piranha solution more efficiently removes PSNPs from the SiO$_2$ matrix. Figure S3 depicts the absorbance spectra and photographs of a PSNP/SiO$_2$ PC sample before and after immersion for 2 days in THF. After THF treatment, the sample opacity visually increases and the FCC diffraction blue-shifts slightly while decreasing in intensity. These results indicate that THF partially and heterogeneously dissolves some of the PSNPs but does not completely remove PS from the SiO$_2$ matrix. We hypothesize that THF is inefficient at removing PS due to the small interpore "window" size that limits solvent and polymer diffusion into and out of the SiO$_2$ matrix, respectively. Piranha solution is an extremely strong oxidizer that efficiently destroys organics, such as PSNPs, while leaving the SiO$_2$ matrix intact. We chose to utilize piranha solution to remove the PSNPs rather than calcination in a 500 °C oven to avoid the partial collapse of the SiO$_2$ matrix, as previously observed by Phillips et al.[17]

Figure 2A shows a photograph of a representative deep UV diffracting IO PC after piranha treatment. This IO PC contains a visually homogeneous region indicated by an arrow that diffracts strongly in the deep UV. Parts B−E of Figure 2 show SEM micrographs of the visually homogeneous region of the IO PC indicated in Figure 2A. The surface of the strongly diffracting region of this IO PC shows a close-packed FCC (111) plane of voids surrounded by the SiO$_2$ matrix remaining after removal of the PSNPs via piranha treatment. At high magnification, up to three subvoid features are visible (Figure 2C) through windows formed in the SiO$_2$ matrix between the top two FCC planes. These windows are formed during self-assembly where direct sphere-to-sphere contact between two FCC planes excludes TEOS and prevents SiO$_2$ condensation. These subvoids indicate that either FCC or hexagonal close packing continues for at least one additional layer for this IO PC.

As shown in Figure 2D at a lower magnification, the top layer of the visually homogeneous region of this IO PC comprises many well-ordered areas several μm^2 in area that are separated by grain boundaries and smaller, disordered regions. We observed negligible cracking throughout the visually homogeneous region of this sample. To study subsurface
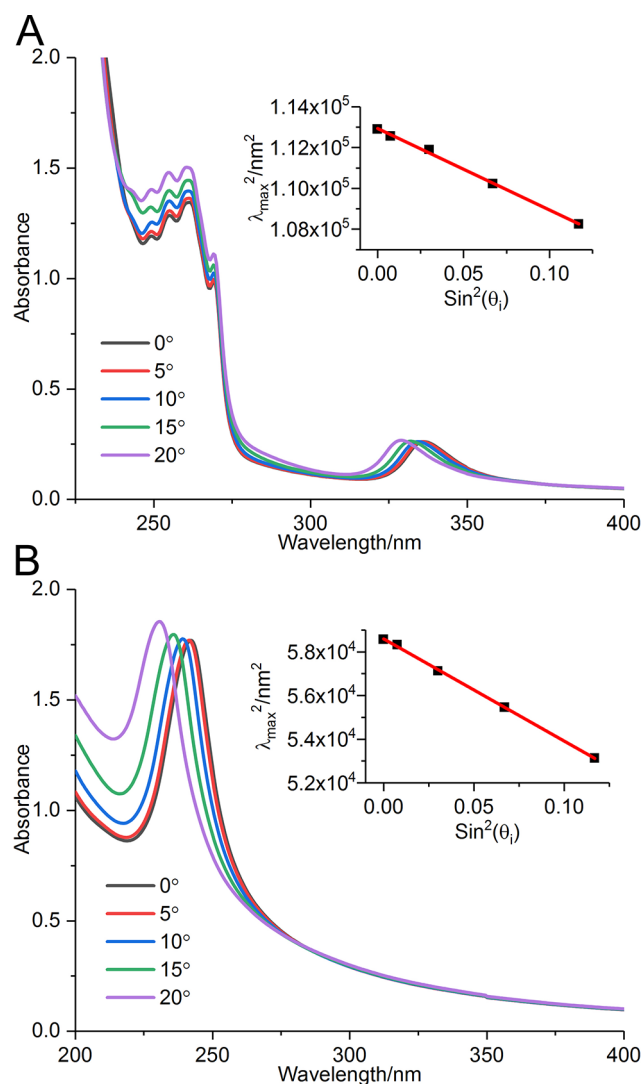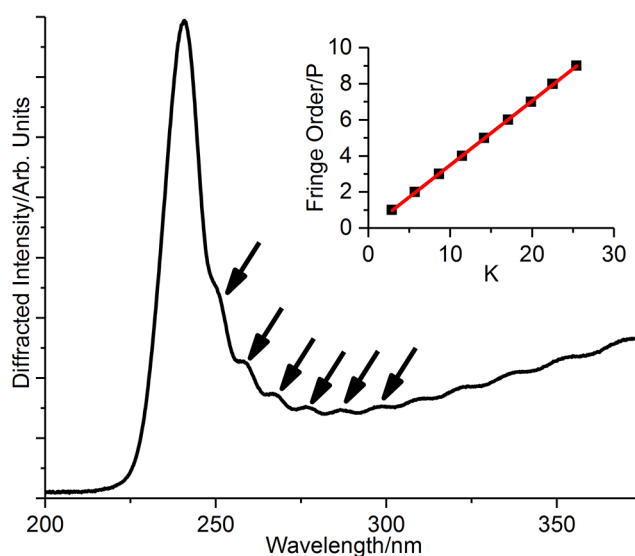
Figure 3. Absorbance spectra measured using the absorption spectrometer of the PC shown in Figure 2. (A) PSNP/SiO$_2$ PC absorbance spectra measured at five incident angles, showing FCC (111) diffraction at ~336 nm and strong PSNP absorption below 275 nm. (B) Absorbance spectra of the same PC at the same incident angles after piranha treatment, yielding an IO PC. The linear fit of λ_{max}^2 versus $\sin^2(\theta_i)$ (inset plots) enables experimental determination of d_{111} and n_{avg}. Listed angles are the incident light angles in air measured from the PC surface normal (θ_i).

Figure 4. LDLS diffraction spectrum of the IO PC shown in Figure 2 at a 15° incidence angle in air. The primary FCC (111) diffraction peak occurs at ~241 nm. Also evident are a number of Fabry−Perot interference fringes, labeled by arrows. Inset: Fabry−Perot fringe plot. $K = (2n_{avg} \cos(\theta_i)(\lambda_1 - \lambda_P)/(\lambda_1 \lambda_P)) \times 10^4$ where $n_{avg} = 1.13$, $\theta_i = 15°$, λ_1 is the wavelength of the longest wavelength interference fringe detectable, in this case at 370 nm, and λ_P is the wavelength of subsequent fringes at shorter wavelengths.

structure and relative ordering of the edges of subsurface layers of the IO PC, we imaged any visible cracks and delaminated areas near the edge of the IO PC substrate (Figure 2E) after mounting the IO PC on a 45° tilt sample mount. The subsurface stacking of the FCC (111) layers parallel to the substrate surface appears excellent, with no evident transitions to body centered cubic (BCC) or hexagonally close packed (HCP) structures within this IO PC.

PC Diffraction via UV−Visible Spectroscopy. After self-assembly, the 3D close-packed PSNP/SiO$_2$ PCs diffract in the near UV according to Bragg's law (eq 1),[22,31]

$$m\lambda = 2n_{avg}d \sin(\theta) \tag{1}$$

where m is the diffraction order, λ is the wavelength of light in vacuum, n_{avg} is the average refractive index of the PC, d is the FCC (hkl) spacing, and θ is the glancing angle within the PC.[32]

Before PSNP removal, the PSNP/SiO$_2$ PCs show an FCC (111) diffraction peak at ~336 nm at normal incidence that is accompanied by strong absorption below 275 nm due to electronic transitions of the PSNPs (Figure 3A). After piranha treatment to remove the PSNPs, IO PCs visually become almost transparent to visible light and the FCC (111) diffraction blue-shifts ~94 nm into the deep UV to ~242 nm at normal incidence (Figure 3B). The FCC Bragg diffraction wavelength can be precisely controlled by tuning the glancing angle of incident light. Entirely different spectral regions can also be selected for diffraction by utilizing different diameter PSNPs during vertical deposition. For example, we utilized smaller diameter PSNPs under identical vertical deposition conditions to produce IO PCs that diffract at 211 nm at normal incidence (Figure S4).

The blue-shifted diffraction upon PSNP removal is expected from Bragg's law due to the decrease in n_{avg} upon removal of the high refractive index PSNPs and their replacement with air. We utilized the method described by Waterhouse et al. to calculate the d_{111} plane spacing and n_{avg} for the PSNP/SiO$_2$ PCs and IO PCs (Figure 3 insets; see Supporting Information for additional details).[13] The FCC d_{111} plane spacing and n_{avg} for six individual PSNP/SiO$_2$ PCs were calculated to be 101.8 ± 2.2 nm and 1.65 ± 0.04 at ~336 nm, respectively. Three of the six PSNP/SiO$_2$ PCs were then treated with piranha to remove the PSNPs, and the measurements were repeated, yielding a calculated FCC d_{111} plane spacing and n_{avg} for the IO PCs of 107.5 ± 2.2 nm and 1.13 ± 0.02 at ~242 nm, respectively.

The ~105 nm d_{111} spacing experimentally determined from Figure 3 is slightly shorter than expected from theory. Assuming a totally close packed structure, a 138 nm particle diameter yields an expected d_{111} of ~113 nm.[32] This smaller

than expected d_{111} spacing is likely due to slight shrinkage of the SiO_2 matrix along the substrate normal (y axis) due to silanol condensation during the PSNP/SiO_2 PC self-assembly, which was previously observed for a similar system by Phillips et al.[17] Using the micrograph shown in Figure 2C, we measure an average void diameter of 137.1 ± 7.2 nm in the zx plane, which is similar to the original PSNP diameter. This result indicates that the IO PC voids likely shrink heterogeneously and only along the substrate normal, in agreement with previously observed behavior.

Although the calculated d_{111} FCC spacing remains approximately constant after piranha solution treatment, there is a sharp reduction in the measured average refractive index of the PC upon PSNP removal. The theoretical PC n_{avg} can be readily calculated by using a weighted average of the refractive indices of each PC material.[6,33] Assuming a close-packed PSNP/SiO_2 FCC PC structure, 74% of the volume contains PSNPs, with a refractive index of 1.62 at 437 nm, the shortest wavelength refractive index we found tabulated for PS.[34] The remaining 26% volume contains an SiO_2 matrix with a refractive index of 1.47 at 437 nm and 1.51 at 240 nm,[35] yielding a theoretical n_{avg} for the PSNP/SiO_2 PC of 1.58 at 437 nm. Assuming complete removal of the PSNPs and replacement with air, with a refractive index of 1.00 at 240 nm, results in a calculated n_{avg} for the IO PC of 1.13 at 240 nm, a ~30% reduction upon PSNP removal. This calculated n_{avg} is in excellent agreement with the measured n_{avg} of 1.13 at ~240 nm. This reduction in the PC n_{avg} upon sphere removal results in a blue-shift of the diffraction wavelength according to Bragg's law.

In addition to the blue-shifted diffraction, the overall attenuation of the incident beam, as measured by the absorption spectrometer, also increases upon PSNP removal due to the increased refractive index contrast between the SiO_2 matrix and air, as expected. Scattering strength, and therefore the efficiency of PC diffraction, is related to the refractive index difference between the surrounding SiO_2 matrix and the PSNPs or air-voids.[36] Removal of the PSNPs and replacement with air increases the refractive index contrast within the PC, yielding much stronger diffraction from the IO PCs compared to the PSNP/SiO_2 PCs. This results in stronger attenuation of incident light at the Bragg condition (Figure 3B).

IO PC LDLS Diffraction. We utilized a LDLS and a deep UV spectrometer to measure the spectrum of Bragg diffracted light from our IO PCs (Figure 4). The LDLS utilizes a tightly focused laser to produce a Xe plasma that emits spectrally broad, bright white light from the far-UV through the near-IR spectral regions. Since plasma formation occurs in a spatially small, point-like area, the Xe plasma emission is easily collimated by using an off-axis parabolic mirror. The resulting output beam is spectrally broad but highly collimated, enabling IO PC diffraction measurements without degradation due to source beam divergence.

A diffraction spectrum of the above IO PC illuminated by the collimated LDLS light is depicted in Figure 4. The most intense peak at ~241 nm is due to FCC (111) diffraction. At longer wavelengths from the FCC (111) diffraction peak, several additional, regularly spaced peaks are visible due to Fabry−Perot interference. Fabry−Perot fringing (etaloning) arises from multiple beam interference by light reflected by the top and bottom faces of the IO PC film and is often visible in IO PC LDLS diffraction spectra.[37] Fabry−Perot fringes have been previously observed for 3D close-packed PCs of visibly

diffracting silica nanospheres.[12] The λ_{max} of each Fabry−Perot fringe can be easily utilized to calculate the thickness of the self-assembled IO PC film (Figure 4 inset). We calculate a thickness of 3558 ± 13 nm, equal to the slope linear fit of the fitted fringe data, for the above IO PC, using the relationships described by Jiang et al.[12] Given a measured d_{111} spacing of 107.5 nm (Figure 3), we calculate that our inverse opal is ~33 layers thick in the center of the strongly diffracting region indicated by the arrow in Figure 2A.

Although we rigorously controlled the light incident angle in both absorbance (Figure 3) and LDLS diffraction experiments (Figure 4), we observe a small ~5 nm difference in the Bragg peak wavelength between these two spectra at the same IO PC rotational angle. We hypothesize that this small difference in Bragg peak wavelength between these two experimental approaches is due to increasing baselines in these spectra that slightly shift the apparent Bragg peak positions. In the collected absorbance spectra (Figure 3) diffuse scattering and slowly increasing absorption by the IO PC SiO_2 matrix cause the transmission to decrease at shorter wavelengths. In the LDLS diffraction spectrum (Figure 4), the baseline increases at longer wavelengths likely due to incomplete deconvolution of the lamp spectrum during spectral processing. We expect that the rising baselines in the absorbance spectra and the LDLS diffraction spectrum slightly blue-shift and red-shift, respectively, the apparent Bragg peak positions. The small shift in the Bragg peak positions between these two techniques negligibly impacts PC parameters calculated using these spectra. For example, the IO PC d_{111} spacing calculated via the absorbance data (107.5 nm, Figure 3B) is in excellent agreement with the d_{111} spacing measured using 229 nm laser diffraction (109 nm, Figure 5); vide infra.
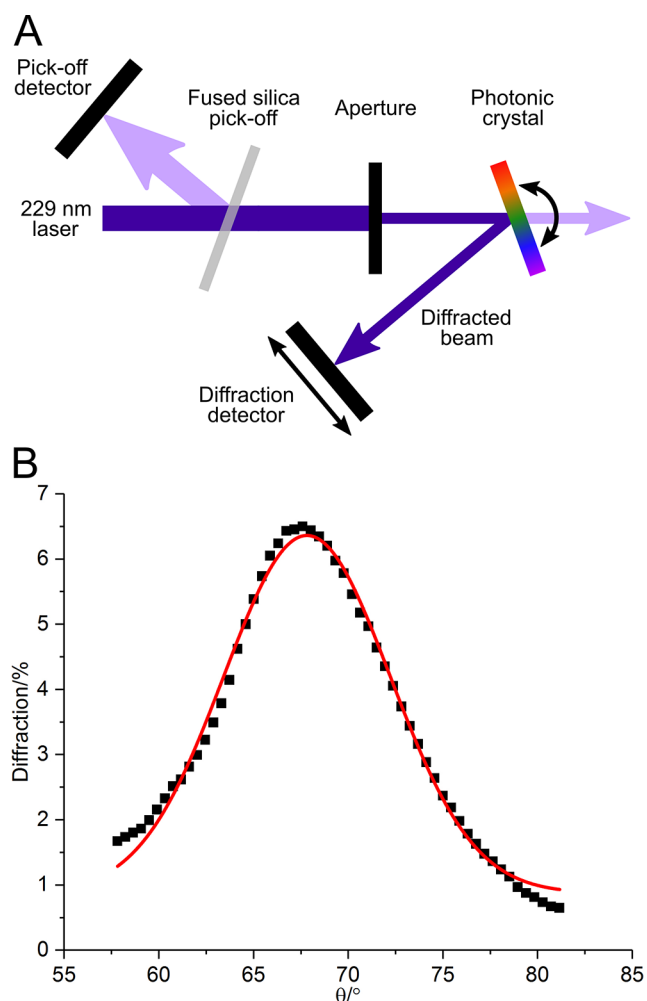
IO PC 229 nm Diffraction. The IO PC diffraction results collected via LDLS illumination provides a convenient way to quantitate the IO PC thickness and to qualitatively assess the FCC Bragg diffraction intensity and bandwidth. To quantitatively determine the IO PC diffraction bandwidth, we measured the intensity of 229 nm laser light diffracted by the IO PC as a function of incident angle, using a more accurate approach based on our previously reported method (Figure 5).[6]

To calculate the diffraction bandwidth, we illuminated an IO PC with collimated 229 nm light while tuning the IO PC rotational angle in 0.50° increments and measuring the power of the diffracted light at each angle with a power meter.

After accounting for refraction by the IO PC, we calculate a glancing angle of maximum diffracted power of 67.8° and a Bragg diffraction full width at half max (FWHM) of 10.3° from the Gaussian fit of the 229 nm diffraction curve. Using our previously described method, we utilized Bragg's law to calculate the d_{111} plane spacing and the FWHM of the diffracted peak in units of wavelength to be 109 and 16.8 nm, respectively. Our 109 nm d_{111} spacing calculated from these 229 nm diffraction data is in excellent agreement with the value calculated for the IO PCs using our absorbance data (Figure 3B).

During these experiments, we observed the transmission and diffraction intensity of the 229 nm beam using fluorescent paper at angles near and far from the Bragg condition. At the Bragg condition, we observe near complete attenuation of the transmitted 229 nm light, indicating strong diffraction. However, we calculate a relatively low maximum diffraction efficiency based on the measured power of the diffracted beam.

Figure 5. (A) Schematic of the 229 nm diffraction experiment layout. (B) Intensity of 229 nm diffraction by the IO PC shown in Figure 2 as a function of Bragg glancing angle, θ, within the IO PC. A Gaussian fit is shown in red.

For the IO PC used to collect the data shown in Figure 5, the diffracted beam appears as an extended line shape (Figure 6A). Much of the line shaped diffracted light missed the power meter head, resulting in a lowered calculated diffraction efficiency.

Rotating the IO PC about the laser beam incident axis (y-axis) rotates the line shaped diffracted beam. The sample orientation dependence of the diffraction likely results from the sample morphology. We studied the morphology of the IO PC shown in Figure 2A in greater detail using an optical profilometer. Optical profilometers measure surface topology via interferometry, producing images depicting the sample surface roughness a function of position. The strongly diffracting area of the sample (Figure 2A, region indicated by arrow) appears homogeneous when observed by eye and via normal incidence SEM. However, when examining the surface topology via optical profilometry, we observe microscopic striations in the sample surface (Figure 6B). The long axes of these semiregularly spaced striations in the sample surface run roughly parallel to the IO PC x-axis. These striations are also weakly visible in SEM micrographs taken when the IO PC is tilted 45° (Figure S5).

We hypothesize that these IO PC surface striations scatter light similarly to irregularly spaced grooves in a diffraction
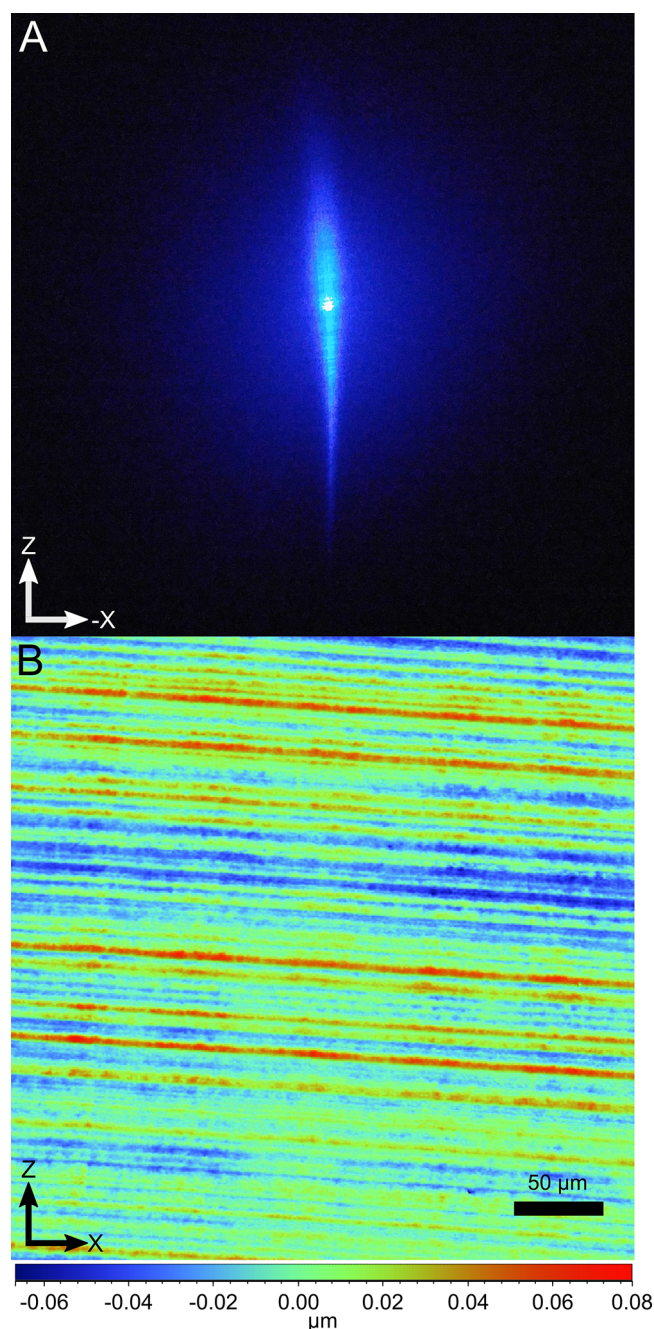
Figure 6. (A) Picture of the 229 nm diffracted beam shape on a luminescent paper viewing screen for the IO PC at a 26.5° IO PC incident angle in air, corresponding to the Bragg condition for 229 nm light. (B) Height map of the strongly diffracting region of the IO PC shown in Figure 2 measured using an optical profilometer. The color-bar depicts the height of surface features, where red and blue map colors indicate raised features and depressions, respectively.

grating. In diffraction gratings, variations in groove spacing and depth are known to produce diffusely scattered light in the grating dispersion plane, perpendicular to the groove long axis.[38] We propose that the semiregularly spaced striations in our IO PC sample surface resemble irregularly ruled grooves in a diffraction grating, producing in-plane diffuse scattering whose long axis is perpendicular to the striation long axis.

These IO PC surface striations lie parallel to the solution surface during vertical deposition. Previous studies have shown that the contact lines of solutions containing dissolved solids

exhibit complicated deformation and pinning behaviors during evaporation.[39,40] In the case of evaporating solutions of nanoparticles, several previous authors have observed the formation of regularly spaced bands of close packed nanoparticles on the substrate that are separated by bare regions containing no nanoparticles,[26,41,42] while others have observed continuous films that have periodic variations in thickness as a function of position.[43] We do not observe alternating areas of bare and nanoparticle covered substrate via SEM in the strongly diffracting region of our IO PC. However, we hypothesize that some meniscus deformation occurs during vertical deposition of the PSNPs onto the fused silica substrate, resulting in the semiregular IO PC surface striations observed using the profilometer and 45° tilt SEM. We are currently investigating methods to mitigate the formation of these surface striations during the vertical deposition self-assembly process to minimize their impact on IO PC diffraction.

The 16.8 nm FWHM diffraction bandwidth measured for this IO PC is relatively broad. We expected that the diffraction bandwidth for these IO PCs would be broader than that of our aqueous PCs due to the relatively large refractive index difference between the air voids and the SiO_2 matrix. Increasing the refractive index contrast within a PC increases the scattering strength of the FCC planes, reducing the number of planes taking part in Bragg diffraction. We previously showed that reducing the number of FCC diffraction planes taking part in PC diffraction broadens the diffraction bandwidth.[32] The diffraction bandwidth of these IO PCs can be reduced by infiltrating solvents or UV-transparent polymers into the air-voids to refractive-index-match the voids to the SiO_2 matrix. Disordered regions of the IO PC also broaden the diffracted bandwidth. We are currently investigating methods to further optimize the modified vertical deposition method to improve IO PC order.

A significant advantage of these solid IO PCs compared to our previous aqueous deep UV diffracting PCs is that they do not depend upon easily disrupted electrostatic interactions between nanoparticles dispersed in solvent to maintain FCC ordering and Bragg diffraction. The solventless SiO_2 FCC structure affords these IO PCs mechanical durability and photochemical stability, enabling them to be repeatedly used and characterized, even under direct laser irradiation. In our previous work, we observed that upon ∼2 mW/cm² 229 nm laser irradiation, the diffraction intensity of our aqueous PCs decreased with time.[6] We illuminated this IO PC with the same 229 nm laser at a 20× higher irradiance of ∼41 mW/cm² and observed no degradation of our IO PC diffraction intensity.

Furthermore, the mechanical durability of these IO PCs allows them to be easily transported and handled. For example, the IO PC depicted in Figure 2 was spectroscopically characterized >10 times and extensively handled for ∼4 months prior to SEM imaging. IO PC absorbance spectra collected before and after this extensive handling are nearly identical (Figure S6), indicating that time, handling, and deep-UV/near-UV/visible irradiation negligibly impact IO PC diffraction.

These indefinitely shelf stable IO PCs enhance the potential utility of deep UV diffracting PC optical devices by enabling their long-term storage and use. Although further development and optimization of the fabrication procedure are necessary in order to improve their diffraction efficiency and to reduce their diffraction bandwidth, the mechanically robust IO PC fabrication method is extremely promising as an approach to develop deep UV diffracting PC optical devices.

CONCLUSION

We demonstrated the first solid IO PCs that diffract in the deep UV at <245 nm. To fabricate these deep UV diffracting IO PCs, we first self-assembled $PSNP/SiO_2$ 3D close-packed FCC PCs by depositing PSNPs onto fused silica substrates in the presence of TEOS solution using a modified vertical deposition method. After studying the diffraction characteristics of the close-packed $PSNP/SiO_2$ PCs in the near-UV, we removed the PSNPs using piranha solution, yielding IO PCs that diffracted at <245 nm. We characterized the diffraction of these IO PCs to determine their utility for use as deep UV optical devices and found that they show large ∼98% attenuations for light that meets the Bragg condition and a 17 nm FWHM diffraction bandwidth. These solid IO PCs show superior mechanical durability, shelf life, and photochemical stability under direct 229 nm laser irradiation compared to our previously demonstrated aqueous based PCs. Further optimization of the vertical deposition procedure is necessary, and we are currently investigating methods to improve IO PC self-assembled order to reduce the diffraction bandwidth and to decrease the surface roughness to improve the shape and efficiency of the diffracted light.

ASSOCIATED CONTENT

⑤ Supporting Information

The Supporting Information is available free of charge on the ACS Publications website at DOI: 10.1021/acsanm.8b01806.

> PSNP synthesis, additional electron micrographs, deep UV absorbance spectra from an IO PC fabricated utilizing smaller diameter nanoparticles, details concerning the method used to calculate important PC parameters, absorbance spectra of a similar PC before and after THF treatment, and a figure demonstrating the long-term stability of the fabricated IO PC (PDF)

AUTHOR INFORMATION

Corresponding Author

*E-mail: asher@pitt.edu.

ORCID ⓘ

Kyle T. Hufziger: 0000-0001-6057-8232
Alyssa B. Zrimsek: 0000-0002-3503-7239
Sanford A. Asher: 0000-0003-1061-8747

ACKNOWLEDGMENTS

■ REFERENCES

(1) Wang, L.; Tikhonov, A.; Asher, S. A. Silica Crystalline Colloidal Array Deep Ultraviolet Narrow-band Diffraction Devices. *Appl. Spectrosc.* **2012**, *66*, 426−431.

(2) Asher, S. A.; Johnson, C. R.; Murtaugh, J. Development of a New UV Resonance Raman Spectrometer for the 217−400-nm Spectral Region. *Rev. Sci. Instrum.* **1983**, *54*, 1657−1662.

(3) Asher, S. A. Ultraviolet Raman Spectrometry. In *Handbook of Vibrational Spectroscopy*; Chalmers, J. M., Griffiths, P. R., Eds.; Wiley, 2002; pp 1−15.

(4) Bykov, S. V.; Sharma, B.; Asher, S. A. High-Throughput, High-Resolution Echelle Deep-UV Raman Spectrometer. *Appl. Spectrosc.* **2013**, *67*, 873−883.

(5) Nelson, M. P.; Treado, P. J. Raman Imaging Instrumentation. In *Raman, Infrared, and Near-Infrared Chemical Imaging*; Sasic, S., Ozaki, Y., Eds.; John Wiley & Sons: Hoboken, NJ, 2011; Chapter 2, pp 23−51, DOI: 10.1002/9780470768150.ch2.

(6) Hufziger, K. T.; Bykov, S. V.; Asher, S. A. Ultraviolet Raman Wide-field Hyperspectral Imaging Spectrometer for Standoff Trace Explosive Detection. *Appl. Spectrosc.* **2017**, *71*, 173−185.

(7) Asher, S. A.; Holtz, J.; Liu, L.; Wu, Z. Self-Assembly Motif for Creating Submicron Periodic Materials. Polymerized Crystalline Colloidal Arrays. *J. Am. Chem. Soc.* **1994**, *116*, 4997−4998.

(8) Asher, S. A.; Kimble, K. W.; Walker, J. P. Enabling Thermoreversible Physically Cross-Linked Polymerized Colloidal Array Photonic Crystals. *Chem. Mater.* **2008**, *20*, 7501−7509.

(9) Lee, H. S.; Shim, T. S.; Hwang, H.; Yang, S.-M.; Kim, S.-H. Colloidal Photonic Crystals toward Structural Color Palettes for Security Materials. *Chem. Mater.* **2013**, *25*, 2684−2690.

(10) Wang, J.; Liang, J.; Wu, H.; Yuan, W.; Wen, Y.; Song, Y.; Jiang, L. A Facile Method of Shielding from UV Damage by Polymer Photonic Crystals. *Polym. Int.* **2008**, *57*, 509−514.

(11) Wong, S.; Kitaev, V.; Ozin, G. A. Colloidal Crystal Films: Advances in Universality and Perfection. *J. Am. Chem. Soc.* **2003**, *125*, 15589−15598.

(12) Jiang, P.; Bertone, J. F.; Hwang, K. S.; Colvin, V. L. Single-Crystal Colloidal Multilayers of Controlled Thickness. *Chem. Mater.* **1999**, *11*, 2132−2140.

(13) Waterhouse, G. I.N.; Waterland, M. R. Opal and Inverse Opal Photonic Crystals: Fabrication and Characterization. *Polyhedron* **2007**, *26*, 356−368.

(14) Jiang, P.; McFarland, M. J. Large-scale Fabrication of Wafer-size Colloidal Crystals, Macroporous Polymers and Nanocomposites by Spin-coating. *J. Am. Chem. Soc.* **2004**, *126*, 13778−13786.

(15) Ye, X.; Qi, L. Two-dimensionally Patterned Nanostructures Based on Monolayer Colloidal Crystals: Controllable Fabrication, Assembly, and Applications. *Nano Today* **2011**, *6*, 608−631.

(16) Bohn, J. J.; Ben-Moshe, M.; Tikhonov, A.; Qu, D.; Lamont, D. N.; Asher, S. A. Charge Stabilized Crystalline Colloidal Arrays as Templates for Fabrication of Non-close-packed Inverted Photonic Crystals. *J. Colloid Interface Sci.* **2010**, *344*, 298−307.

(17) Phillips, K. R.; Vogel, N.; Hu, Y.; Kolle, M.; Perry, C. C.; Aizenberg, J. Tunable Anisotropy in Inverse Opals and Emerging Optical Properties. *Chem. Mater.* **2014**, *26*, 1622−1628.

(18) Hatton, B.; Mishchenko, L.; Davis, S.; Sandhage, K. H.; Aizenberg, J. Assembly of Large-area, Highly Ordered, Crack-free Inverse Opal Films. *Proc. Natl. Acad. Sci. U. S. A.* **2010**, *107*, 10354−10359.

(19) von Freymann, G.; Kitaev, V.; Lotsch, B. V.; Ozin, G. A. Bottom-up Assembly of Photonic Crystals. *Chem. Soc. Rev.* **2013**, *42*, 2528−2554.

(20) Stein, A.; Wilson, B. E.; Rudisill, S. G. Design and Functionality of Colloidal-Crystal-Templated Materials—Chemical Applications of Inverse Opals. *Chem. Soc. Rev.* **2013**, *42*, 2763−2803.

(21) Li, C.; Qi, L. Bioinspired Fabrication of 3D Ordered Macroporous Single Crystals of Calcite from a Transient Amorphous Phase. *Angew. Chem., Int. Ed.* **2008**, *47*, 2388−2393.

(22) Hufziger, K. T.; Bykov, S. V.; Asher, S. A. Raman Hyperspectral Imaging Spectrometer Utilizing Crystalline Colloidal Array Photonic Crystal Diffraction. *Appl. Spectrosc.* **2014**, *68*, 1219−1223.

(23) Reese, C. E.; Guerrero, C. D.; Weissman, J. M.; Lee, K.; Asher, S. A. Synthesis of Highly Charged, Monodisperse Polystyrene Colloidal Particles for the Fabrication of Photonic Crystals. *J. Colloid Interface Sci.* **2000**, *232*, 76−80.

(24) Wang, L.; Zhao, X. Fabrication of Crack-free Colloidal Crystals Using a Modified Vertical Deposition Method. *J. Phys. Chem. C* **2007**, *111*, 8538−8542.

(25) Shimmin, R. G.; DiMauro, A. J.; Braun, P. V. Slow Vertical Deposition of Colloidal Crystals: A Langmuir−Blodgett Process? *Langmuir* **2006**, *22*, 6507−6513.

(26) Kaplan, C. N.; Wu, N.; Mandre, S.; Aizenberg, J.; Mahadevan, L. Dynamics of Evaporative Colloidal Patterning. *Phys. Fluids* **2015**, *27*, 092105.

(27) Prevo, B.; Velev, O. Materials Deposition in Evaporating Menisci—Fundamentals and Engineering Applications of the Convective Assembly Process. In *Evaporative Self-Assembly of Ordered Complex Structures*; Lin, Z., Ed.; World Scientific Publishing Co.: Singapore, 2012; pp 109−155, DOI: 10.1142/9789814304696_0003.

(28) Born, P.; Munoz, A.; Cavelius, C.; Kraus, T. Crystallization Mechanisms in Convective Particle Assembly. *Langmuir* **2012**, *28*, 8300−8308.

(29) Yang, L.; Gao, K.; Luo, Y.; Luo, J.; Li, D.; Meng, Q. In Situ Observation and Measurement of Evaporation-Induced Self-Assembly Under Controlled Pressure and Temperature. *Langmuir* **2011**, *27*, 1700−1706.

(30) Meng, L.; Wei, H.; Nagel, A.; Wiley, B. J.; Scriven, L. E.; Norris, D. J. The Role of Thickness Transitions in Convective Assembly. *Nano Lett.* **2006**, *6*, 2249−2253.

(31) Carlson, R. J.; Asher, S. A. Characterization of Optical Diffraction and Crystal Structure in Monodisperse Polystyrene Colloids. *Appl. Spectrosc.* **1984**, *38*, 297−304.

(32) Asher, S. A.; Weissman, J. M.; Tikhonov, A.; Coalson, R. D.; Kesavamoorthy, R. Diffraction in Crystalline Colloidal-Array Photonic Crystals. *Phys. Rev. E* **2004**, *69*, 066619.

(33) Pan, G.; Sood, A. K.; Asher, S. A. Polarization Dependence of Crystalline Colloidal Array Diffraction. *J. Appl. Phys.* **1998**, *84*, 83−86.

(34) Sultanova, N.; Kasarova, S.; Nikolov, I. Dispersion Properties of Optical Polymers. *Acta Phys. Pol., A* **2009**, *116*, 585−587.

(35) Malitson, I. H. Interspecimen Comparison of the Refractive Index of Fused Silica. *J. Opt. Soc. Am.* **1965**, *55*, 1205−1209.

(36) Bertone, J. F.; Jiang, P.; Hwang, K. S.; Mittleman, D. M.; Colvin, V. L. Thickness Dependence of the Optical Properties of Ordered Silica-air and Air-polymer Photonic Crystals. *Phys. Rev. Lett.* **1999**, *83*, 300.

(37) Hecht, E. *Optics*, 3rd ed.; Addison Wesley Longman, 1998.

(38) Palmer, C. A.; Loewen, E. G. *Diffraction Grating Handbook*; Newport Corporation: Rochester, NY, 2005.

(39) Deegan, R. D.; Bakajin, O.; Dupont, T. F.; Huber, G.; Nagel, S. R.; Witten, T. A. Contact Line Deposits in an Evaporating Drop. *Phys. Rev. E: Stat. Phys., Plasmas, Fluids, Relat. Interdiscip. Top.* **2000**, *62*, 756−765.

(40) Adachi, E.; Dimitrov, A. S.; Nagayama, K. Stripe Patterns Formed on a Glass Surface During Droplet Evaporation. *Langmuir* **1995**, *11*, 1057−1060.

(41) Abkarian, M.; Nunes, J.; Stone, H. A. Colloidal Crystallization and Banding in a Cylindrical Geometry. *J. Am. Chem. Soc.* **2004**, *126*, 5978−5979.

(42) Watanabe, S.; Inukai, K.; Mizuta, S.; Miyahara, M. T. Mechanism for Stripe Pattern Formation on Hydrophilic Surfaces by Using Convective Self-Assembly. *Langmuir* **2009**, *25*, 7287−7295.

(43) Lozano, G.; Míguez, H. Growth Dynamics of Self-Assembled Colloidal Crystal Thin Films. *Langmuir* **2007**, *23*, 9933−9938.